Title Assessment of non X-ray background in the X-IFU.

Prepared by : S. Lotti, C. Macculi, V. Fioretti  Date : 09/01/2019

Inputs by : Date :

Checked by : A. Argan  Date : 09/01/2019

Agreed by : D. Brienza  Date : 09/01/2019

Authorized by: L. Piro  Date : 09/01/2019

DISTRIBUTION LIST

X-IFU consortium
ESA

DOCUMENT CHANGE RECORD

Issue	Date	Changed Section	Description of Change
1	09/01/2019		1st Issue

Abbreviations and acronyms

Item	Meaning
AIT	Assembly Integration and Test
ASI	Agenzia Spaziale Italiana
ASW	Application Software
CADM	Configuration and Data Management
CNR	Consiglio Nazionale delle Ricerche
CPO	Central Project Office
CryoAC	Cryogenic Anticoincidence
FA	Funding Agency
FEE	Front End Electronics
FPA	Focal Plane Assembly
GSE	Ground Segment
ICU	Instrument Control Unit
INAF	Istituto Nazionale di Astrofisica
LPO	Local Project Office

MP	Management Plan
OBS	Organization Breakdown Structure
PA	Product Assurance
PBS	Product Breakdown Structure
PS	Project Scientist
SM	System Manager
UniGE	University of Genova
UniPA	University of Palermo
WBEE	Warm Back End Electronics
WBS	Work Breakdown Structure
WEE	Warm Electronics
X-IFU	X-ray Integral Field Unit

Applicable Documents

[AD#]	Doc. Reference	Issue	Title
[AD1]			

Reference Documents

[RD#]	Doc. Reference	Issue	Title
[RD1]	http://geant4.web.cern.ch/		Geant4: a simulation toolkit
[RD2]	AREMBES Geant4		AREMBES WP 7: Normalization of an isotropic flux in space in Geant4 simulations
[RD3]	TN_INAF_GCR_2018_001		GCR flux assessment for the ATHENA X-IFU particle background evaluation
[RD4]	https://doi.org/10.1002/2016JA022920		Empirical model of long-time variations of galactic cosmic ray particle fluxes

[RD#]	Doc. Reference	Issue	Title
[RD5]	Exp Astron (2012) 33:39–53 DOI 10.1007/s10686-011-9269-7		The radiation environment in L-2 orbit: implications on the non-X-ray background of the eROSITA pn-CCD cameras
[RD6]	Arembes TN 4.1		Arembes TN 4.1: Software Implementation of Radiation Transport and Effects Models
[RD7]	Technical report RI OAS/2/2018		ATHENA/X-IFU Geant4 simulation: cut-off optimization
[RD8]	Exp Astron (2017): DOI 10.1007/s10686-017-9538-1		The particle background of the X-IFU instrument
[RD9]	TN_INAF_GCR_2018_001	1	GCR flux assessment for the ATHENA X-IFU particle background evaluation
[RD10]	TN_INAF_HTM_2018_001	1	Validation of the HITOMI SXS particle background by Geant4

Table Of Contents

1. Introduction

No X-Ray mission has ever flown to L2, thus it is impossible to estimate the expected background level relying on existing data. The problem is also too complex to face using an analytical approach, and consequently the background estimates are performed using Monte Carlo simulations with the Geant4 software [RD1].

Geant4 is a toolkit that provides access to several different models to reproduce physical processes the user is interested in. Also, it is possible to set the simulation detail level to suit the user needs, balancing the accuracy of the results with the simulation speed.

Thanks to this tool it is possible to recreate a virtual model of the instrument and its surroundings (the so-called Mass Model) and of the particle environment it will be placed into, and analyze how they interact with each other and ultimately, given the proper settings, to predict the expected instrument performances, among which the background level.

Furthermore, it is possible to test the effect of changes to the instrument mass model (sensitivity analysis) and identify the configuration that optimizes the detector performances

2. Simulation settings and normalization procedure

There are several models in the Geant4 toolkit that treat the same physical processes, with different internal settings and applicability conditions. Which models to use, and their internal settings, are defined in the so-called Physics List file. The Geant4 consortium provides several pre-assembled Physics Lists, optimized for different purposes.

We started the background evaluation activity using the pre-assembled Physics List that according to software developers was the most suited for space-based applications, namely the G4EmStandardPhysics_option4 (Opt4).

However, given the number of physical applications Geant4 can be used to simulate, it is impossible to validate the software behavior in every possible situation. So, thanks to ESA support, in the context of a Core Technology Program (CTP) called “AREMBES” (ESA Contract No. 4000116655/16/NL/BW) we started an activity aimed to pinpoint the most suited physical models and settings to simulate the Athena detectors behavior in space. We defined our own Physics List dedicated to Athena, the “Space Physics List” (SPL), comparing the performances of different Geant4 models in reproducing the available experimental data for the physical processes involved in the generation of background [RD6]. At the end of this activity the SPL was officially endorsed by ESA for the X-IFU, and we adopted it as our reference settings for Athena simulations.

We then compared the effect of the two physics lists on the simulation results, using as inputs the same GCR protons spectrum [RD3] and the same mass model and the 4.9.2 version of the Geant4 software. The results are shown in Figure 1, and show that there is a ~23% reduction on the simulation results resulting from the software settings.

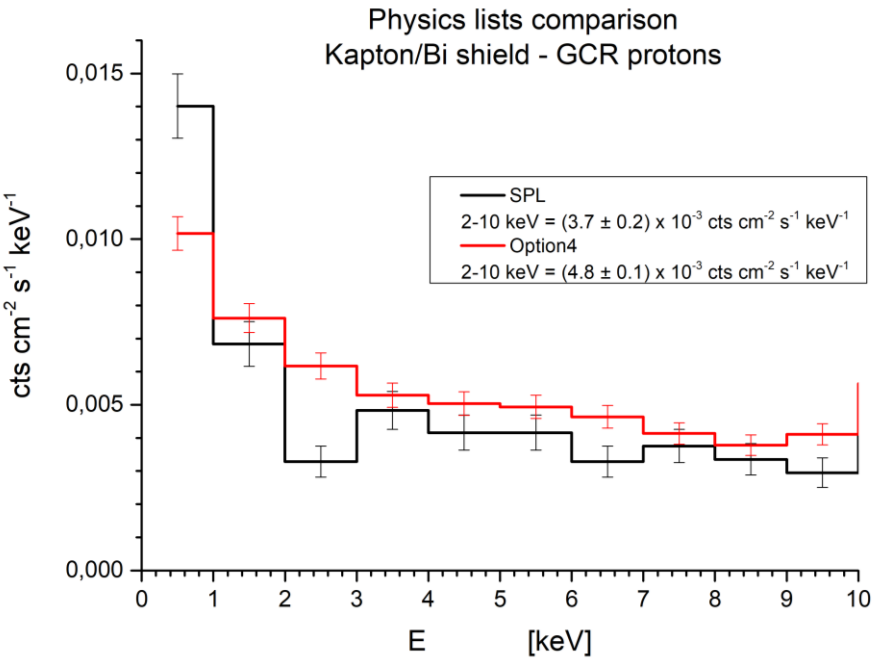

Figure 1. Residual background level obtained with the two physics lists described in the text.

In the standard configuration the different solids in the mass model are assigned to different regions within Geant4, each with different settings of the cutoff[1] for the generation of secondary particles:

- The detector, the supports, and the surfaces directly seen by the detector were assigned to the "inner region" with the lowest possible cut values (few tens of nm, high detail level)
- The remaining solids in the FPA were assigned to an "intermediate region" with higher cut values (few μm)
- The cryostat and the masses outside the FPA were assigned to the "external region" were the cut (few cm) allowed the creation only of high energy secondary particles

We tested also the dependence of the background on the cutoff value of the different regions [RD7]. Regarding the inner region, we found out that increasing the cut for gammas, e-, and e+ from 0.05 μm to 0.5 μm allows a decrease of the total CPU time of about 60% without losing precision in the background simulation. The use of the Space Physics List, without the single scattering, gives consistent results, within the errors, with the rates obtained using the reference Opt4 physics list, while increasing the CPU time of about 30-40%. All results are summarized in Figure 2.

[1] The cutoff defines the energy threshold below which secondary particles are not created and traced by the simulation.

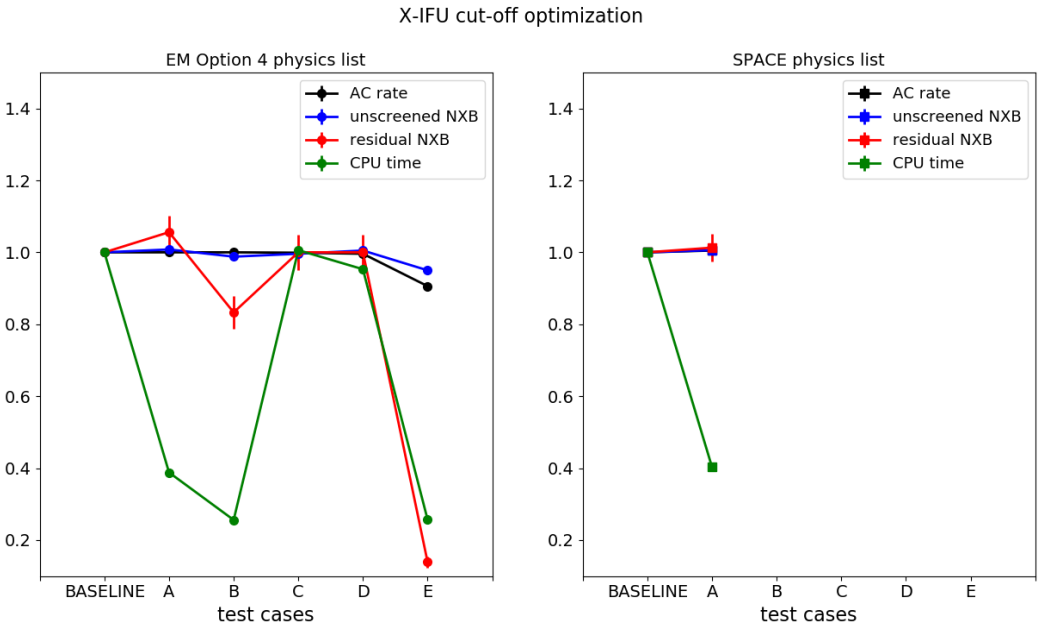

Figure 2. Summary of the resulting rates and CPU times, relative to the BASELINE test case.

The normalization procedure of the simulations, namely the process that leads from the number N of emitted particles to a particle or count rate, has been recently defined in [RD2]. The simulated exposure time T (in seconds) to the isotropic flux depends on the number of simulated particles N as follows:

$$T = \frac{N}{\varphi \times 4\pi^2 R_{ext}^2 \times \sin^2 q} \text{ seconds.}$$

Where we assume that the particles are emitted from a spherical surface of radius R_{ext} within a cone of half angle (q), following a cosine law angular distribution (see Figure 3), and where φ is the energy integrated particle intensity in space, in units of particles cm^{-2} s^{-1} sr^{-1},

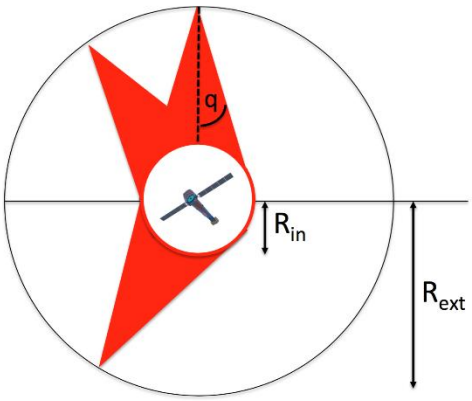

Figure 3. Schematic view of the angular and geometrical distribution of the input particles.

3. Baseline configuration

Without any kind of reduction technique the X-IFU would experience a GCR-protons induced background level of (185 ± 0.1) × 10^{-3} cts/cm^2/s/keV in the 2-10 keV energy band, 37 times above the 5 × 10^{-3} cts/cm^2/s/keV requirement (see Figure 4). For this reason, a cryogenic anticoincidence detector (CryoAC) was introduced in the baseline configuration. This allowed to reduce the unrejected background level down to (6 ± 0.2) × 10^{-3} cts/cm^2/s/keV, efficiently discriminating against high energy particles that can cross the detector and reach the CryoAC, but still 20% above the requirement. This evaluation was performed taking into account only GCR protons (which produce ~ 80% of the residual particle background), while in Section 4 (see Figure 9) we will report the expected full contribution.

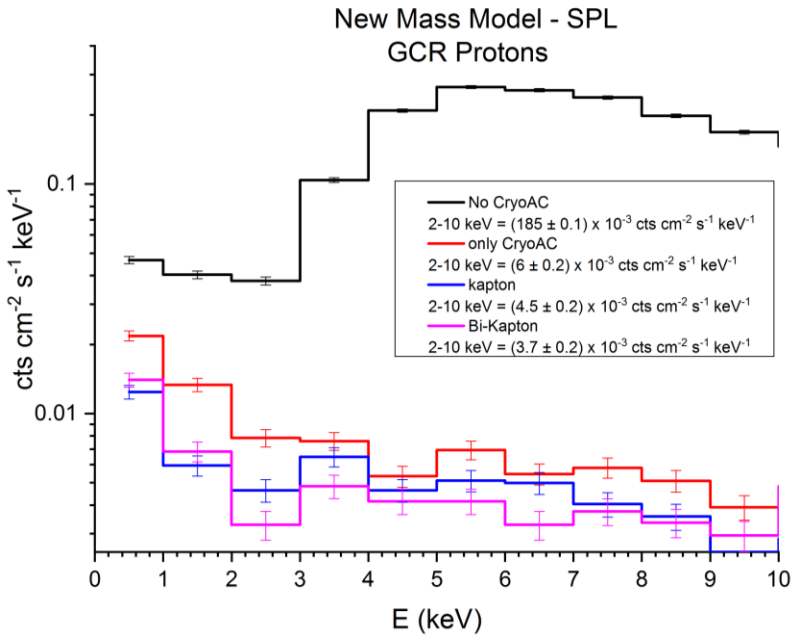

Figure 4 – background levels in different FPA configurations.

The analysis of the residual background composition and origin revealed that this background level was induced mainly by secondary electrons coming from the niobium shield surrounding the detector that impact the X-IFU from above and backscatter on its surface, releasing a small fraction of their energy (see Figure 7 – left and Figure 8). To reduce this component, we decided to test the secondary electrons yield from different materials, and designed a passive low-Z shield to interpose between the detector and the Niobium. This Kapton shield introduction allowed to further damp the residual background level induced by GCR protons down to (4.5 ± 0.2) × 10^{-3} cts/cm^2/s/keV.

After the Kapton insertion, the background showed a significant contribution (~10%) from 16 and 18 keV Niobium fluorescence lines that induce escape peaks on the detector. To prevent these fluorescence photons from reaching the detector several improvements to the passive shielding were tested [RD8], and finally the best

option for the passive shield was found to be 10 um of Bismuth followed by 250 um of Kapton, that allowed to reach the level of $(3.7 \pm 0.2) \times 10^{-3}$ cts/cm^2/s/keV.

These background levels were obtained applying different screening strategies:

- Time coincidence with the CryoAC: photons are not expected to produce a coincidence signal in the X-IFU-CryoAC system, so we can assume that every event that is detected simultaneously ($\Delta t < 10$ us) in both the CryoAC and the main detector can be rejected as particle-induced one. A CryoAC threshold of 20 keV is considered.
- Pattern recognition: due to the detector features (no charge cloud diffusion among different pixels as in CCD-like detectors, pixels physically separated) source photons will not produce complicate pixel patterns to reconstruct. Instead we can assume that all the events that turn on more than one pixel can be rejected as induced by particles with skew trajectories intersecting more than one pixel, or simultaneous impacts by multiple particles.
- Energy deposition: given the steep decrease of the optics effective area outside the detector energy band, we can assume that all the events that deposit energies outside the instrument sensitivity band are due to charged particles and, therefore, reject them.

4. Sensitivity analysis:

On 9/5/2017 and on 23/5/2017 we have received the updated model drawings of both the cryostat from CNES and the FPA from SRON, respectively, from which we have derived an updated version of the Geant4 mass model (see Figure 5).

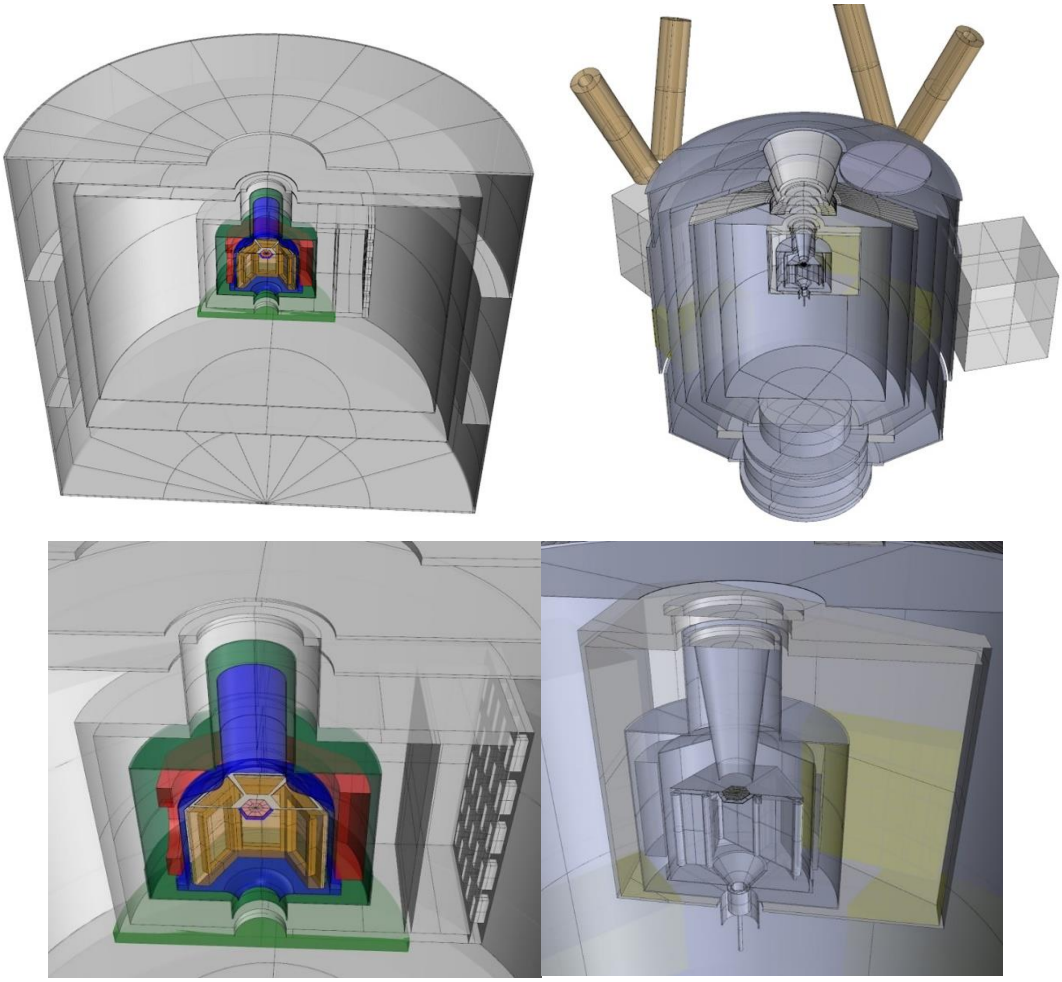

Figure 5 - The old and new cryostat mass models (top left and right, respectively) and FPA (bottom left and right).

With respect to the previous mass model, beside the revision of the structures surrounding the detector, we have:

- updated the TES absorbers thicknesses from 4 μm to 4.2 μm for Bismuth, and from 1 μm to 1.7 μm for Gold
- inserted a more realistic model of the thermal filters, and the aperture cylinder sustaining them

Despite all the modifications to the simulation setup, the background level resulting from the GCR protons component was not affected sensibly (the variation on the residual particle background is ~ 10 %, see Figure 6).

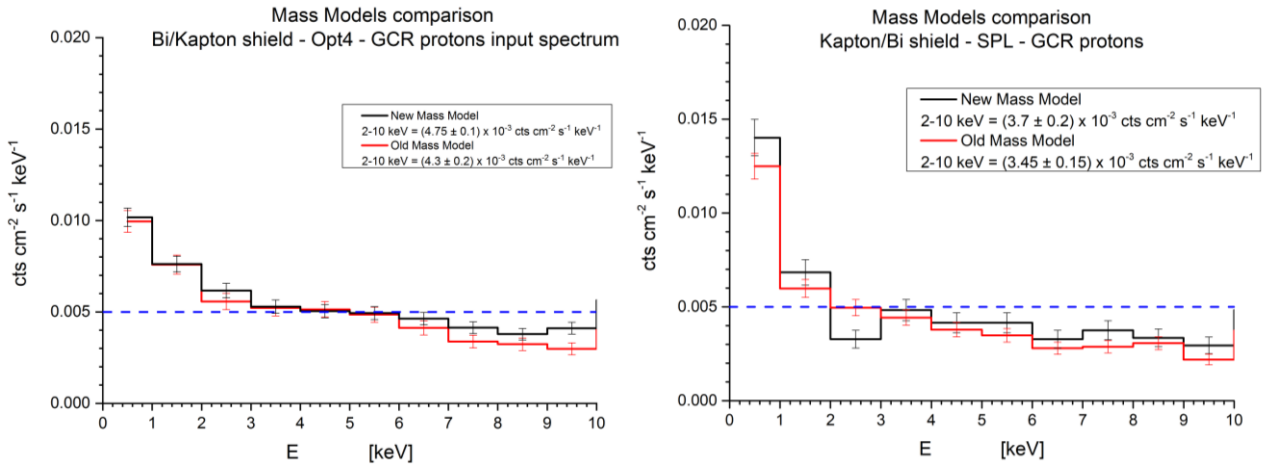

Figure 6 - The residual background spectra from the GCR protons, obtained with the old and new mass models using the Opt4 and SPL physics lists.

The structures in direct sight of the detector (i.e., the Kapton/Bi passive shield and the Niobium shield) are the only ones that were not substantially modified, thus this result shows that the unrejected background value is quite robust to changes in the mass model that may happen far from the detector.

We investigated the geometrical origin of the unrejected background resulting from the GCR protons component, and the results are reported in Figure 7. On the left the background origin obtained without the insertion of the passive shield for electrons, while on the right the same plot after introducing the Kapton/Bi shield. Before the shield introduction the major fraction of the background is induced by the 50 mK Niobium shield, being this the last surface directly seen by the detector (Figure 7 – left). After the Kapton/Bi insertion the contribution from this surface is now mostly blocked by the passive shield, going from ~80% contribution to 12% (Figure 7 – right). Even though now the passive shield became the relative main background source, due to a lower electron production yield the absolute background level has been reduced.

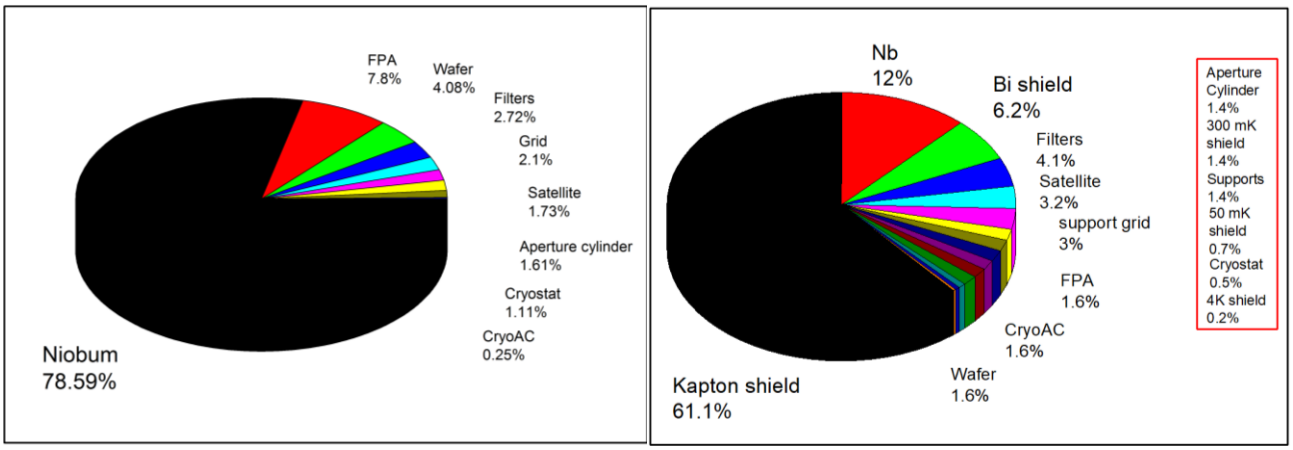

Figure 7 - The residual background origin without passive shielding (left), and after the insertion of the Kapton/Bi shield (right).

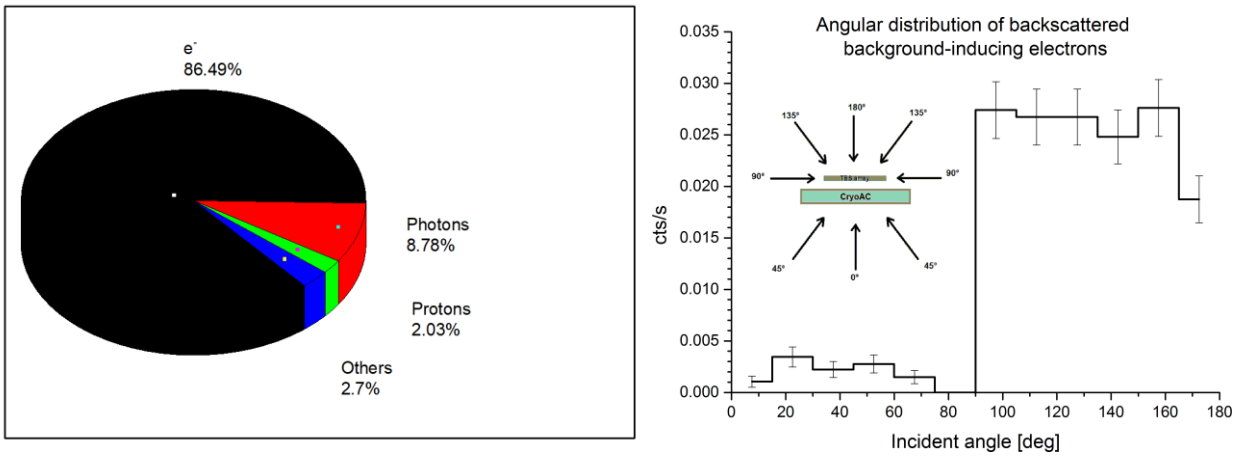

Figure 8 - The residual background composition (left), and the angular distribution of incident directions of the backscattered electrons component (right).

Regarding the background particle composition, backscattered electrons produced in the surfaces directly seen by the detector have repeatedly proven to be the main component of the residual background after the insertion of the CryoAC, since ~85% of the residual background is induced by secondary electrons, and ~80% of these electrons are backscattered Figure 8 (left). Moreover, we were able to produce an angular distribution of the backscattered electrons. These particles impact on the detector surface and bounce back, releasing a small fraction of their energy (dependent on the impact angle). As it can be seen from Figure 8 (right), almost no electrons backscatter on the lower side of the detector, as the CryoAC efficiently blocks/vetoes those particles, while the major contribution comes from above, as expected. The distribution itself is quite flat, indicating no preferential direction from where these electrons come from, aside from a dip around the direction normal to the detector surface. An analysis of the FPA geometry reveals that this is roughly the FoV opening angle, the direction where there is almost no mass to produce the secondary electrons.

Using the updated mass model in the baseline configuration (Kapton/Bi passive shield) we investigated the impact on the background of the other environmental particle populations expected to be present in L2, namely GCR alphas [RD4] and electrons [RD5].

Our analysis reported a total background level (GCR protons, alpha particles and electrons) of $(4.64 \pm 0.26) \times 10^{-3}$ cts/cm^2/s/keV in the 2-10 keV energy band, compliant with the scientific requirement (at less than 2 sigma statistical errors).

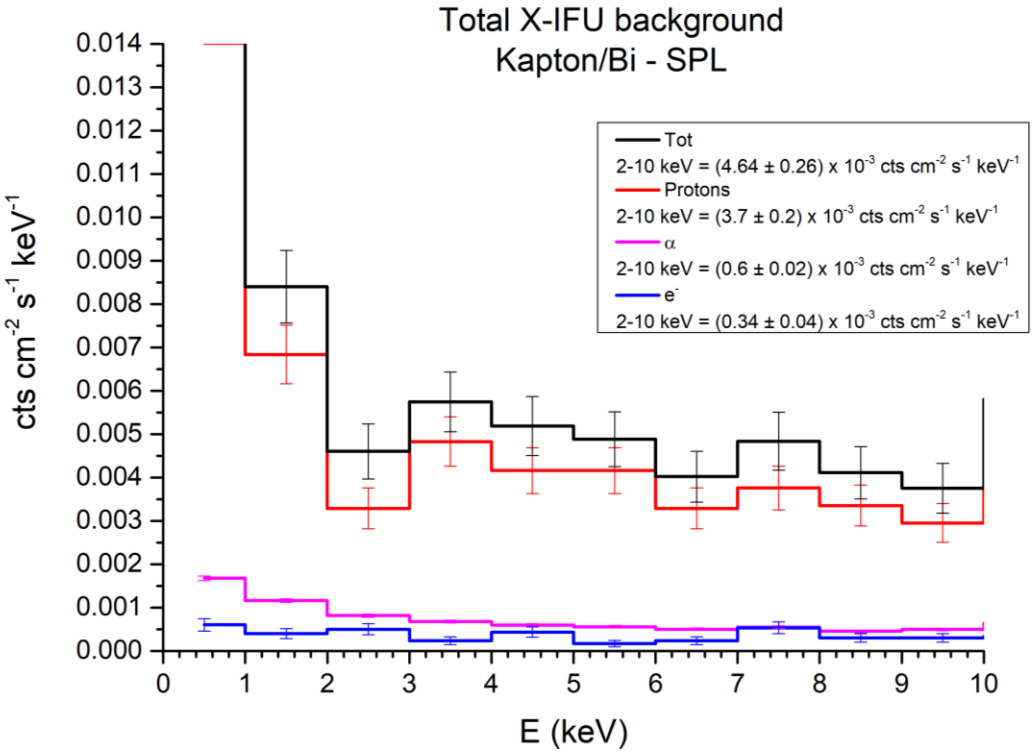

Figure 9 - The unrejected particle background of the X-IFU instrument (black line), and all its contributions: GCR protons (red line), alpha (magenta line) and electrons (blue line).

Inserting additional information regarding the initial energy of the particles able to reach the detector we were able to identify the energy ranges in which the different particle populations are contributing to the background (see Figure 10). We can see that heavier particles require higher energies to be able to reach the innermost part of the cryostat.

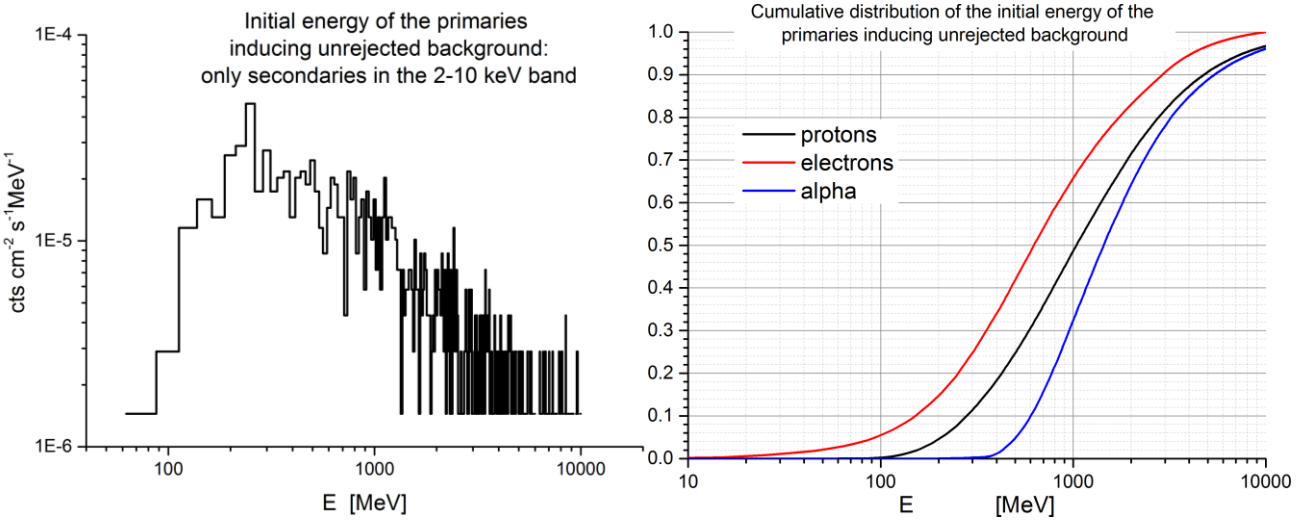

Figure 10 – The initial energy of the primary particles inducing unrejected background, either directly or through the production of secondary particles (left). The cumulative plot of the curve on the left, for GCR protons, alpha particles and electrons (right).

We also investigated the effect of specific changes of the FPA, namely:

- removing the Bismuth layer out of the passive electron shield, leaving only 250 μm of Kapton as in the previous baseline configuration. We report the result of this study in Figure 11.

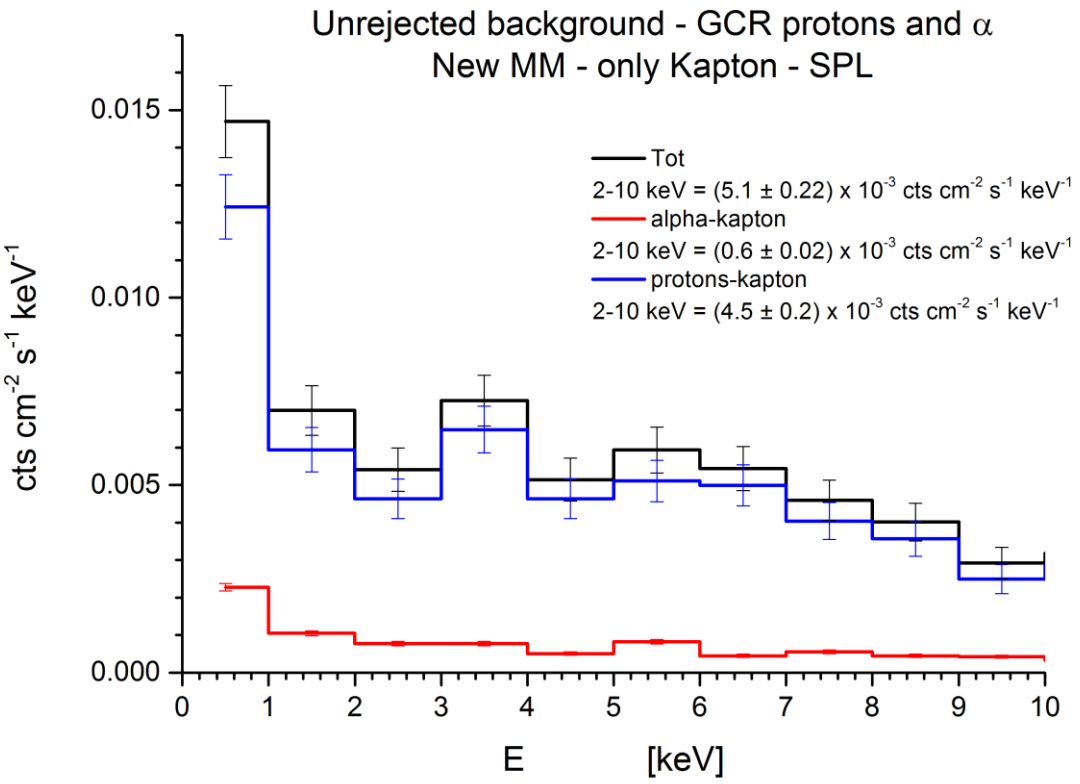

Figure 11 - Unrejected particle background in case of Kapton shielding configuration.

By rescaling the result from the Kapton/Bi assessment (see Figure 9), it is possible to evaluate the 2-10 keV in-band energy integrated contribution due to the GCR electrons, thus having an assessment of the full unrejected particle background in case of only Kapton shielding configuration. The contribution from the GCR electrons is $(0.392 \pm 0.057) \times 10^{-3}$ cts/cm^2/s/keV. Being in general the GCR electrons contribution negligible with respect to the total one (see Figure 9), the result of this scaling can be considered a safe action in assessing the total unrejected background for the Kapton only shielding. The evaluated full unrejected particle background in case of only Kapton is $(5.49 \pm 0.30) \times 10^{-3}$ cts/cm^2/s/keV, not compliant with the scientific requirement (at less than 2 sigma statistical errors).

- Modifying the thicknesses of the Kapton layer of the passive shield and of the Niobium shield inside the allowed ranges (see Figure 12). Regarding Niobium, the unrejected background level was not influenced modifying the thickness from 500 µm to 300 µm. Regarding Kapton, increasing the thickness to 500 µm did not allow for any improvement of the background level, while reducing it down to 100 µm reduced the shielding efficiency of the Kapton layer, slightly increasing the unrejected background level.

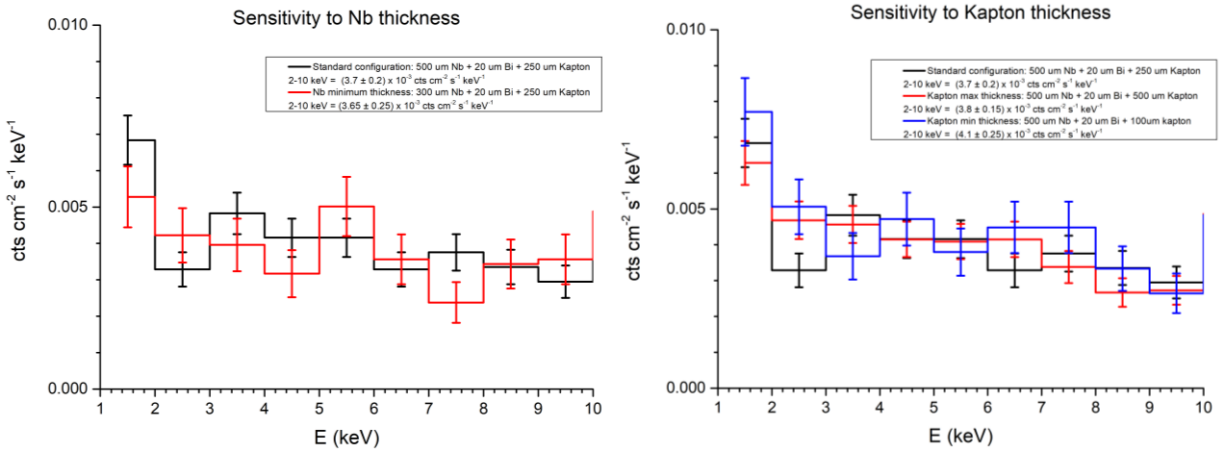

Figure 12. Unrejected background sensitivity to the Niobium (left) and Kapton (right) thicknesses.

- Substituting the Bismuth layer with a Gold one. This was done since Bismuth is a difficult material to handle, while Gold ductility can relatively easily allow to model it into the required shape with few microns thickness. We calculated the required thickness to stop Niobium fluorescences to be 10 µm and simulated the GCR protons induced background, and results are shown in Figure 13.

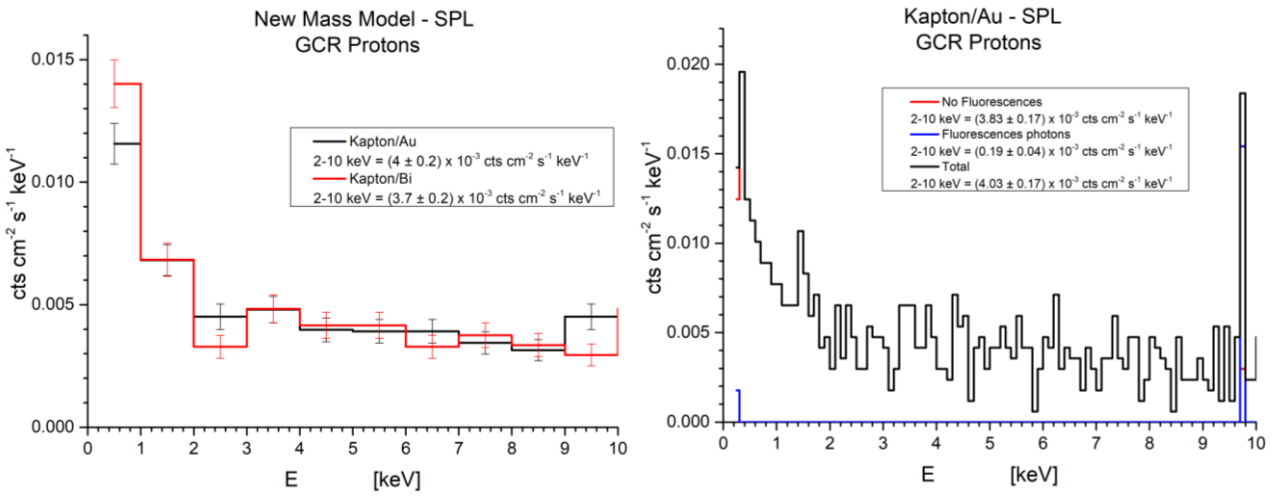

Figure 13. Unrejected particle background in the Kapton/Au shield configuration, compared with the baseline Kapton/Bi configuration (left). A more detailed analysis reveals that the difference in the integrated background value is due to the presence of the gold fluorescence line (right).

The unrejected background level in the Kapton/Au configuration is compatible with the one obtained in the baseline configuration if we remove the additional fluorescence line due to the presence of Gold. It

should be noted that, given the narrow width of the fluorescence line and the extreme energy resolution of the X-IFU, removing the fluorescence line from the background spectrum should pose no issue, resulting in the exclusion of few bins in the response matrix of the instrument (few eV). If the fluorescence line is not removed from the spectrum, the background level increases by ~8%, still inside 1 σ error.

- Increasing the distance between the detector surface and the lower edge of the Kapton/Bi shield.
  In the baseline configuration the Kapton/Bi shield extends beyond the Niobium funnel (the Nb lower edge has a 19 mm distance from the detector surface) down to a distance of 0.25 mm, thus covering almost the whole solid angle the detector is exposed to (the geometry is shown in Figure 14). This distance does not allow enough space for the detector wiring, so we tested how the residual background is affected by its increase.

  We tested several shield distances, and the results are reported in Figure 15. What we found is that the background increases proportionally to the fraction of solid angle left uncovered by the shield.

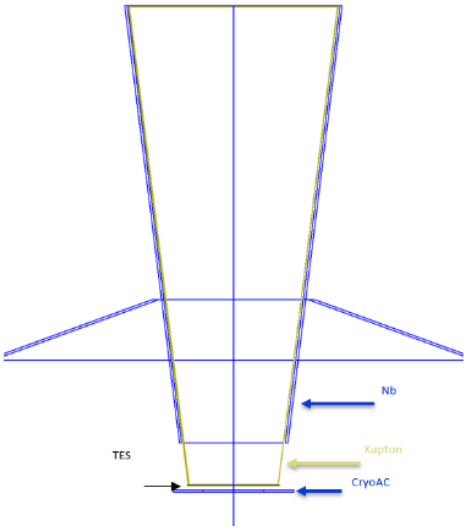

Figure 14. Drawing of the geometry in the detector proximity.

It should be noted that this issue can be mitigated adding a Kapton/Bi layer to the sections of the internal wall of the niobium that the detector became directly exposed to.

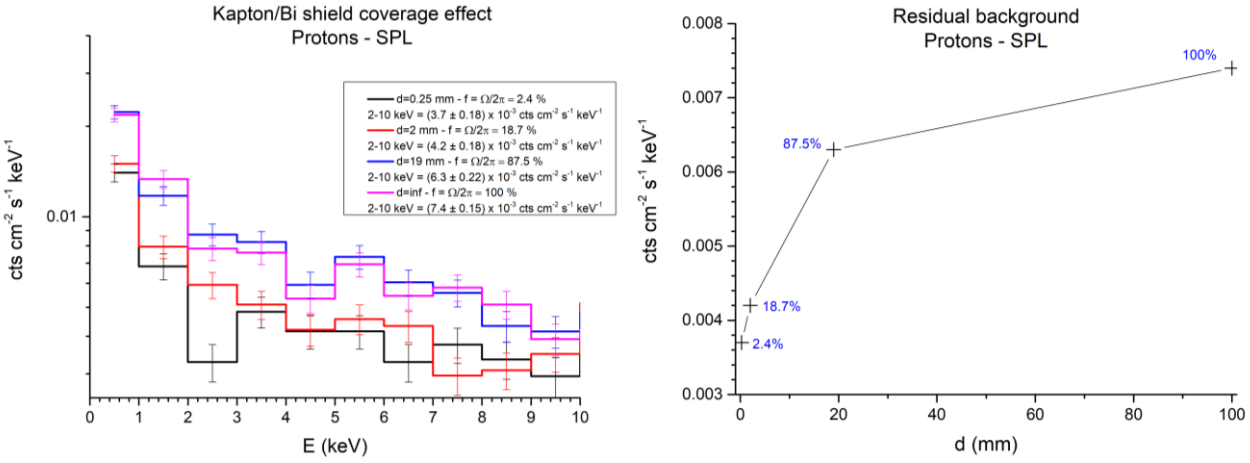

Figure 15. Unrejected particle background in the Kapton/Bi configuration, for different distances of the shield from the detector surface (left). Integrated background level as a function of detector-shield distance (right).

5. Particle fluxes on the detector and CryoAC rejection efficiency

To identify both the CryoAC and the main detector required rejection efficiency in discriminating background events we must first calculate the expected particle fluxes on the detector. This has been done in Figure 16 for all the particle species expected in the L2 environment, separating the primary and secondary particles contribution. For completeness we report both the incident and deposited energy spectra on the main detector array and on the CryoAC, while in Figure 17 we report the spectra of incident energies on the silicon wafer supporting the main detector array.

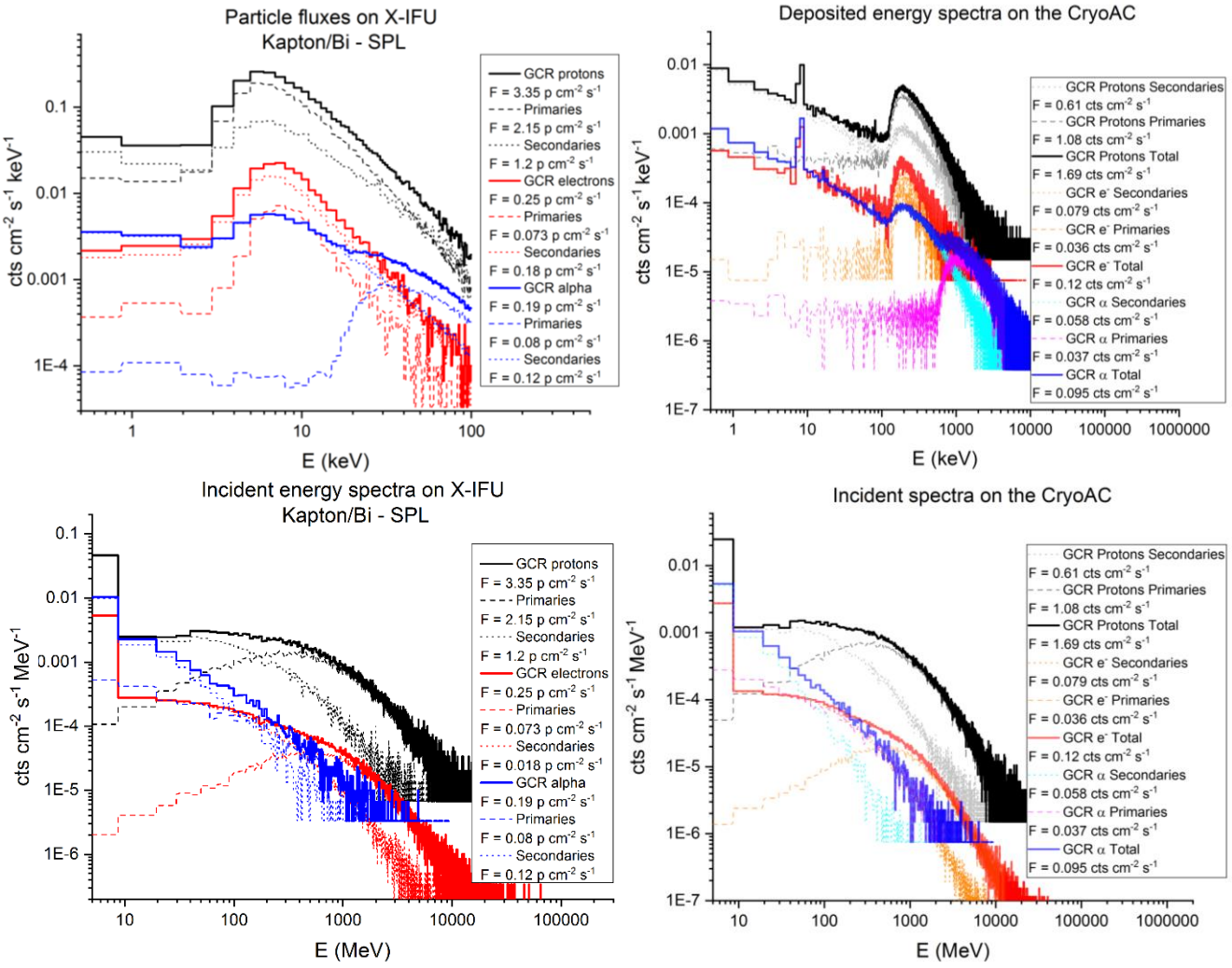

Figure 16. Top left: Deposited energy spectra and integrated fluxes in the main detector (Area=2.3 cm²). Top right: Deposited energy spectra and integrated fluxes in the CryoAC (Area=10.23 cm²). Bottom panels: incident energy spectra on the two detectors, main detector (bottom left panel, Area=2.3 cm²) and CryoAC (bottom right, Area=10.23 cm²); these energies are the ones possessed by the particles before interacting with the detectors.[2]

[2] TES array detector area to be considered is the top surface, since the particle flux is to be compared to source photons flux. The CryoAC area is the whole surface area (top + bottom + side) since it is the flux definition. See the [RD2] for further details and complete justification.

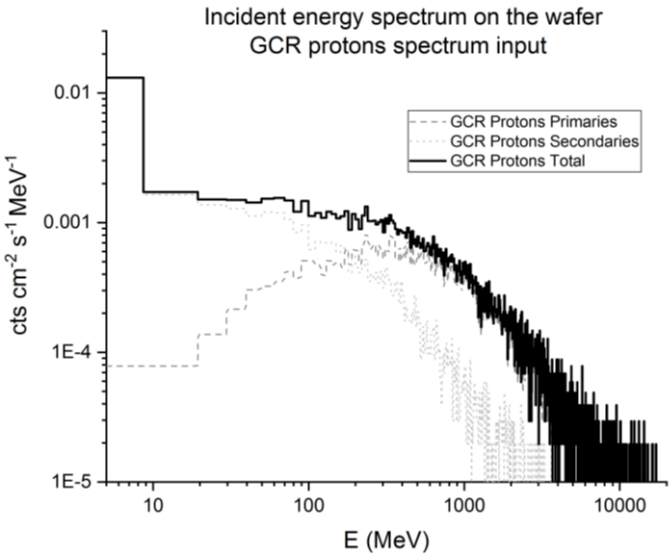

Figure 17. Spectra of incident energies of the particles impacting the silicon wafer supporting the main detector array (GCR protons only).

We expect a total count rate from primary particles of 5.28 cts/s. We require this component to impact the residual background no more than 1/10 of the requirement, i.e., 5 x 10^{-4} cts/cm^2/s/keV in the 2-10 keV band, or 9.2 x 10^{-3} cts/s. To reduce this flux down to the required level we require a total rejection efficiency for primary particles of ~99.83%.

We remark here that the CryoAC rejection efficiency has to be calculated on the primaries component, that is entirely rejectable, and can be validated experimentally. For completeness we report below also the numbers relative to secondary particles, that will not be used in the following analysis, since they are significantly affected by factors such as the FPA and Cryostat mass model or the simulation software settings, that are subject to changes.

Analogously we have a total count rate from secondary particles of 3.44 cts/s. However, a fraction of this flux is induced by unrejectable particles (i.e., electrons backscattering on the detector surface releasing just a fraction of their energy, low energy particles that are completely absorbed inside the main array switching on only one pixel). It cannot be required of the CryoAC and main array to veto these events, so a requirement on the rejection efficiency should be placed only on the rejectable component of the secondary particles flux. The rejectable fraction of the secondary particles count rate amounts to 3.36 cts/s, and as for the primaries case we require this component to impact the residual background no more than 1/10 of the requirement, 9.2 x 10^{-3} cts/s. This sets the total rejection efficiency for rejectable secondary particles to ~99.73%.

The rejection efficiency of the X-IFU system depends on the geometrical configuration of the CryoAC and main array ("geometrical rejection efficiency", depending on distance and sizes of the two detectors) related to the classical concept of the anticoincidence solid angle covering optimization with respect to the main detector, and on the capability of the main array to discriminate background events on its own, relying on the energy deposited and on the pixel pattern turned on by the impacting particles ("detector rejection efficiency").

About the geometrical configuration, an analysis has been performed on:

- the CryoAC vs main detector related distance.

- the CryoAC area with respect to the main detector area

We estimated these efficiencies as function of the geometrical configuration, and the results are reported in Figure 18. The results are related only to the primary component, that is entirely rejectable. Furthermore, to increase the statistics of the simulations, a reduced mass model of the instrument had to be created, and thus the secondary particles population, though not interesting for this analysis as stated above, impacting on the 2 instruments is not representative of the one experienced in the complete model.

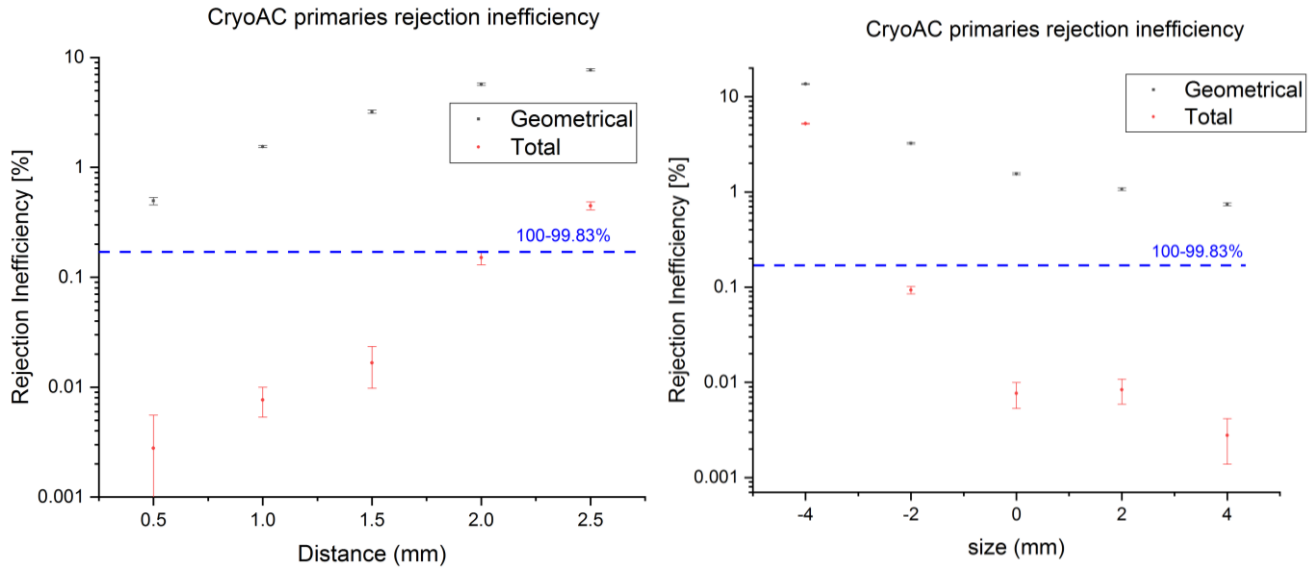

Figure 18. Geometrical and total rejection inefficiency for primary particles (defined as the unity residual of the efficiency) as function of the distance between the main detector and the CryoAC (left), and as function of the CryoAC size increment with respect to the baseline size of 11.91 mm apothem (right). We show inefficiency rather than the efficiency for clarity purpose.

As it can be seen in Figure 18, the geometrical rejection efficiency increases with the solid angle covered by the CryoAC. A 1.5 mm distance is enough to achieve the 99.83% total rejection efficiency goal. We adopt the 1 mm distance solution to account for some margin. Similarly, the baseline CryoAC size is sufficient to reach the goal (Figure 18, right), while further increase in the CryoAC size can be technically challenging with minor benefits. The total rejection efficiency saturates beyond a given CryoAC size/distance, since we start discriminating events with very skew trajectories, that are already intrinsically discriminated by the detector rejection efficiency.

Once the geometry of the system has been defined, we investigated the effect of the energy threshold of the CryoAC on its detection efficiency. In Figure 19**Errore. L'origine riferimento non è stata trovata.** we plot the residual background for the rejectable component (primary particles and secondaries). This is necessary since the primary component, despite being completely rejectable, constitutes a minor fraction of the residual background, so the secondaries contribution can't be neglected. The red line is the requirement for both primaries and secondaries (we have set 5 x 10^{-4} cts/cm^2/s/keV in the 2-10 keV band for each component, thus two times 4 x 10^{-3} cts/cm^2/s). A 20 keV threshold fulfills the requirement. Lowering further the threshold value produces no appreciable benefit, while the unrejected background value starts to rise steeply above 30 keV.

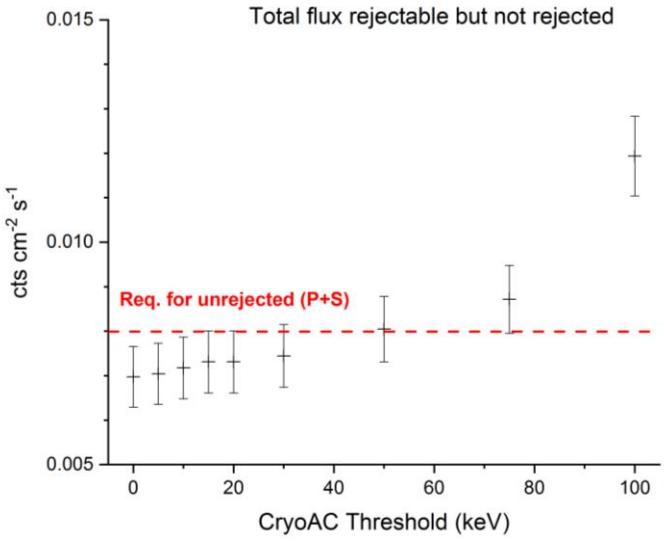

Figure 19. the flux of rejectable particles that are not rejected by the CryoAC in the Kapton-Bi configuration described in Section 3, as function of the low energy threshold. The horizontal red line is the requirement for the rejectable component of the background.

6. Expected variations during mission lifetime

We investigated the expected variations of the unrejected background level during the mission lifetime according to [RD3]. We simulated both the maximum and minimum GCR spectra expected in the 2028 – 2033 period (Figure 20 - left) on the latest version of the X-IFU mass model, and obtained the results shown in Figure 20 (right).

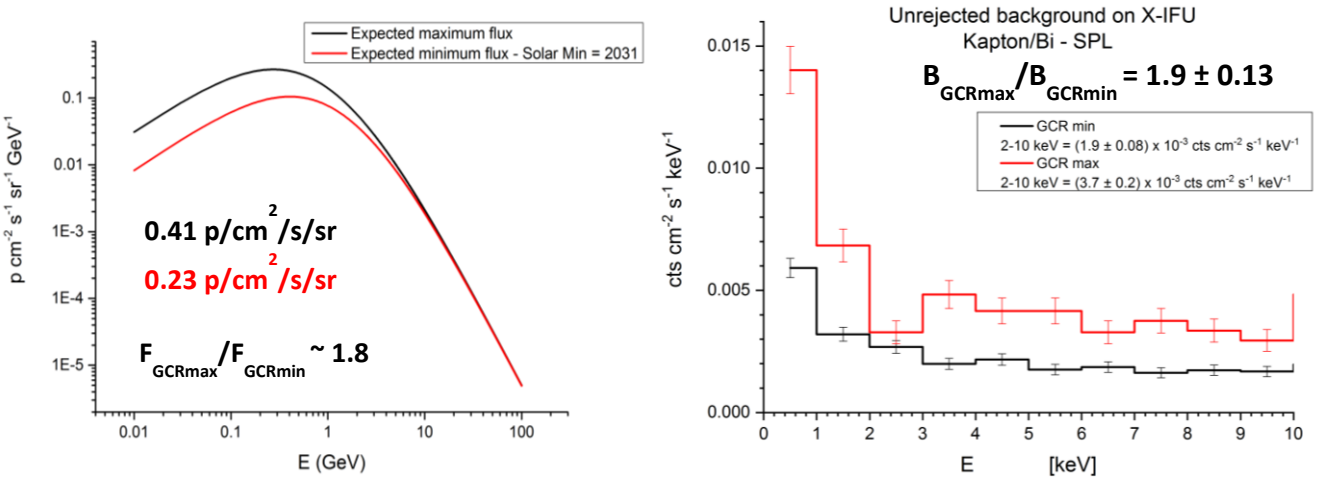

Figure 20. Expected input spectra for the GCR maximum and minimum during Athena mission lifetime (left). Unrejected background spectra resulting from the input spectra on the left (right). Integrated fluxes refer to the 100 MeV – 100 GeV energy band.

The spectral shape of the unrejected background in the 2-10 keV energy band was not affected sensibly by the change in spectral shape, and the integrated value scaled linearly with the integrated fluxes in the 100 MeV – 100 GeV energy band.

7. X-IFU Breakdown on uncertainties

In section 4 we reported the expected total background level that will be experienced by the X-IFU in flight. Despite this can be considered a conservative estimate, assuming that in 2031 Athena will experience a GCR flux level similar to the highest flux ever measured, we need estimate the uncertainty level associated to this value.

There are several sources of uncertainty in the simulation results, namely:

- We expect a ~26 % variation (1 sigma sample variance) of the maximum GCR flux protons [RD9]. The residual background scales approximately linearly with the incident flux (see Section 6), so this can be translated directly into a ~26 % uncertainty on the residual background level. By considering the population variance, the expected variation can be up to six times larger than the above sample variance at 95% CL [RD9].
- Changing the collection of physics models and settings in the Geant4 simulation from Option4 physics list to the Space Physics List (SPL) developed for Athena in the AREMBES framework [RD6], the simulation result changed by ~ 22%. Having been endorsed by ESA, we take as reference the result obtained with SPL (since it has been tuned to reproduce the experimental data for the physical processes involved in the background generation). A ~22 % uncertainty can be assigned to the software settings.
- We have recorded ~ 10% variation by a change in the received X-IFU mass models (see Figure 6).
- The statistical error on the simulation results, given by the pure statistic of the simulation, that amounts to ~ 6% (1 sigma).

We have performed a validation activity on the Hitomi satellite data [RD10], in order to verify how much the approach used for X-IFU can reproduce the background measured by a real microcalorimeter in orbit. The philosophy used in the construction of the Hitomi SXS simulation is the same used for the X-IFU, despite the radiation environment being different. We remark that, despite the origin of particles is different, their interaction with matter is clearly the same.

The results showed that applying the same recipe for the creation of Geant4 simulation and post-processing data analysis used for X-IFU, we are able to reproduce 80% of the measured count rates for both the microcalorimeter and the anticoincidence detector, providing validation for several aspects of the simulation, namely:

- physics list,
- normalization algorithm,
- post processing for the simulation output,
- cut-off settings for secondary particle production

8. Future updates of the X-IFU mass model

The reported results are based on an X-IFU mass model developed from CAD delivered by CNES and SRON on 2017. In particular, the FPA has been slightly modified. This is the reason why a sensitivity analysis has been performed on some items. The main present differences are:

1. the necessity to change the Bismuth in Gold as a second layer of the passive liner (Kapton based)
2. 50 mK filter placed at the bottom of the Nb shield and not at the top)
3. the lower edge of the passive liner must be at a minimum distance higher than 2 mm

Bullets 2 and 3 have a direct impact onto the FPA design. Thanks to the sensitivity analysis performed, we have solutions to mitigate the impact of these differences to the residual particle background: it is again the use of a well-shaped Kapton/gold liner both around the 50 mK filter metallic frame, and on the inner cylindrical surface of the Nb shield. A new set of Geant4 simulation will be performed once the FPA design becomes more mature.